VISUALISATION AND LES SIMULATION OF CAVITATION CLOUD FORMATION AND COLLAPSE IN AN AXISYMMETRIC GEOMETRY

Manolis Gavaises, Fabio Villa and Phoevos Koukouvinis
School of Engineering and Mathematical Sciences, City University London, Northampton Square, EC1V 0HB, London, UK

Marco Marengo
Department of Mechanical Engineering, University of Brighton, UK

Jean-Pierre Franc
LEGI, Grenoble University, BP 53, 38041 Grenoble Cedex 9, France

ABSTRACT

Visualization and Large Eddy Simulations (LES) of cavitation inside the apparatus previously developed by [1] for surface erosion acceleration tests and material response monitoring are presented. The experimental flow configuration is a steady-state closed loop flow circuit where pressurised water, flowing through a cylindrical feed nozzle, is forced to turn 90 degrees and then, move radially between two flat plates towards the exit of the device. High speed images show that cavitation is forming at the round exit of the feed nozzle. The cavitation cloud then grows in the radial direction until it reaches a maximum distance where it collapses. Due to the complexity of the flow field, direct observation of the flow structures was not possible, however vortex shedding is inferred from relevant simulations performed for the same conditions. Despite the axisymmetric geometry utilized, instantaneous pictures of cavitation indicate variations in the circumferential direction. Image post-processing has been used to characterize in more detail the phenomenon. In particular, the mean cavitation appearance and the cavity length have been estimated, showing good correlation with the erosion zone. This also coincides with the locations of the maximum values of the standard deviation of cavitation presence. The dominant frequency of the 'large-scale' cavitation clouds has been estimated through FFT. Cloud collapse frequencies vary almost linearly between 200 to 2000Hz as function of the cavitation number and the downstream pressure. It seems that the increase of the Reynolds number leads to a reduction of the collapse frequency; it is believed that this effect is due to the agglomeration of vortex cavities, which causes a decrease of the apparent frequency. The results presented here can be utilized for validation of relevant cavitation erosion models which are currently under development.

Keywords: cavitation, erosion, collapse, LES

1. INTRODUCTION

Understanding and controlling cavitation has been a major challenge in engineering for many years. Cavitation erosion is generally believed to be the result of violent collapses of the flowing cavitation micro-bubbles within very short time scales [2]; it often leads to vibration and damage of mechanical components, for example, marine propellers and rudders, bearings, fuel injectors, pumps and turbines. Studying the sheet/cloud cavitation is important to understand the causes of cavitation erosion, and to predict accurately its aggressiveness in terms of erosion risks, or even more, damage rate. In [3] a review of the physical mechanisms for cavitation erosion loads is given. These mechanisms are evaluated with observations on the detailed dynamics of the flow over a cavitating hydrofoil and with observations that are available from ships where cavitation has led to erosion damage on the rudder or the propeller. Many recent studies (selectively [1, 4-14]) have examined the time dependent progression of cavitation erosion for different materials. Due to the aforementioned detrimental effects of cavitation on hydraulic equipment, most of experimental research has focused over the years on methods with which cavitation damage could be quantified and linked to measurable material properties. In [15], systematic cavitation erosion tests have been performed on a water hydraulic system; results from this study have been reported in the past and have been widely used for benchmarking relevant computational fluid dynamics and cavitation erosion models. Briefly, it was shown that cavitation erosion during the incubation period was occurring via pitting. Cavitation damage was not correlated with the elastic limit determined from conventional tensile tests and it is conjectured that other parameters such as the strain rate might play a significant role. However, the flow details associated with the erosion tests have not been recorded.

At the same time, many studies have been reported on flow visualisation in cavitating flows in a number of devices. A review on numerical and experimental investigation of sheet/cloud cavitation was carried out by[16]. Sheet/cloud cavitation could influence the dynamic flow pattern. In [17] a numerical and experimental investigation of sheet/cloud cavitation on a hydrofoil at a fixed angle of attack is reported. The results show that, for the unsteady sheet/cloud cavitating case, the formation, breakup, shedding, and collapse of the sheet/cloud cavities increase the turbulent intensity, and are important mechanisms for vorticity production and modification. Another important feature of the problem is the lift oscillations due to the highly periodic nature of the sheet/cloud cavitation. In [18] it was found that the dynamic characteristics of the cavitation vary considerably with various combinations of angle of attack and cavitation number, σ. At higher angles of attack, two types of flow unsteadiness are observed. At low σ, there is a low frequency shedding of cloud cavitation observed at a Strouhal number of about 0.15. This non-dimensional number is relatively insensitive to changes in σ. As σ is raised, the sheet frequency varies almost linearly with cavitation number.

A recent study by [19] was focused on the simultaneous observation of cavitation structures and erosion, in order to find a pattern linking the evolution of cavities with the erosion development. The studies were conducted in a cavitating Venturi nozzle section, where part of the nozzle was covered by a thin aluminium foil; this enabled the rapid accumulation of erosion pits and allowed the observation of the erosion development, since the rest nozzle walls were transparent. From the observations, it was concluded that, while the exact volume and distance of the vapour cavity does not play a significant role to erosion damage, extensive erosion was caused by the collapse of uneven and asymmetrical vapour cavities. The authors hypothesize that erosion might be caused by two mechanisms (or a combination of both): a) the shock wave generated by the cloud collapse is triggering the collapse of microbubbles in the vicinity of the wall area b) the irregular shape of the cavitation cloud causes asymmetrical, non-spherical shock waves that have a distinct orientation.

Along these directions, a number of computational studies on cavitation have been reported over the years. Direct numerical simulation of the whole process is computationally very demanding but provides a good insight into the relevant mechanisms and physics. One notable example of a DNS study of the collective bubble collapse is the recent work of[20], where the authors employed massive parallelism to simulate a cluster of 15,000 bubbles collapsing near a wall, utilizing a grid with size of 13 trillion cells. Of course the resources required to run such a simulation are prohibitive for industrial application; for the specific application the authors utilized a supercomputer consisting of 1.6 million cores, which obviously is impractical to use in everyday engineering computations.

Another approach to simulate the effects of erosion is by including the exact behaviour of the fluid, using a complicated equation of state that reproduces the phase diagram of the liquid/vapour phases. This approach has been followed in[21], who employed a density based solver with shock capturing schemes to simulate the cavitation in the same geometry described in the current paper. Erosion is predicted in the form of shock waves, which originate from the collapse of vapour structures. The simulation methodology, though, had the limitation of small time steps, due to the inclusion of compressibility effects for both liquid and vapour phases.

Considering the above, it becomes obvious that, even if there are state of the art methodologies capable of potentially accurate representation of the behaviour of cavitation structures, their application in everyday problems is limited, due to vast amount of computational resources they require. Thus, in practice, a significant effort is put to derive semi-empirical models to describe the cavitation erosion, which is inherently related to the micro scale effects. Typically, the large-scale problem can be addressed by e.g. multi-phase RANS/LES solvers while the micro-scale problem can be addressed by either a numerical model [22, 23], or by a semi-empirical erosion model or damage functions [24-26]; along these lines, validation against experimental erosion data is of significant importance. Here it should be highlighted that various researchers [24, 27, 28] have found that traditional URANS models suffer from a deficiency in predicting the shedding frequency of cavitating flows; the proposed methodologies to treat this deficiency is either to modify the turbulent viscosity formulation of the traditional URANS models, or employ hybrid RANS/LES or pure LES methodologies.

The present contribution aims to provide more insight to the details of the cavitation sheet/cloud developing in a purpose build device that has been previously used for extensive cavitation erosion measurements[15]. In this paper the same apparatus is used to visualise the cavitating flow in an effort to correlate the observed cavitation erosion locations with the location of cavitation development. The next section of the paper gives a short description of the experimental apparatus used, followed by a brief description of the computational model; then the presentation of the obtained results follows while the most important conclusions are summarised at the end.

2. EXPERIMENTAL SETUP

As already mentioned, the experiments were conducted in a cavitation flow loop described in detail in[15]. The test section is axisymmetric and made of a straight feed nozzle with 16mm diameter. The flow is accelerated by two converging nozzles with cross-section ratios of 2.86:1 and 2.12:1 and lengths 178 and 80mm respectively. As illustrated in Fig. 1, the flow is deflected by the sample to be eroded which is set at a distance of 2.5mm from the nozzle exit. It then moves radially within the 2.5mm gap formed between the sample and the nozzle exit orifice. The radius of curvature of the feed nozzle exit was 1mm. The working fluid was tap water kept at fixed temperature of 25^{o}C. Cavitation erosion data are only available for a cavitation number of 0.9, showing three distinct and clearly separated cavitation erosion sites: two at the upper surface and one of the lower surface. On the upper surface, cavitation erosion is observed just at the turning location of the flow where cavitation is generated and then a few mm further downstream. A cavitation erosion free zone between them exists. On the lower surface, erosion has been observed only at the closure region of the cavity in the form of a circular ring whose mean radius is around 25mm[15].

The test section is placed in a closed circuit comprised by different equipment: centrifugal pump, heat exchanger, test section, electromagnetic flowmeter. The centrifugal pump of 80kW is driven by a variable speed motor. It can provide a pressure of 40bars and a maximum flow of 11l/s. The flow through the system is measured using an electromagnetic flow meter. A heat exchanger allows maintaining the water temperature constant. The maximum operating pressure of the circuit is 40bars, which corresponds to a mean velocity of 65m/s at the turn located at the nozzle exit, calculated at the peripheral surface of the cylinder with height 2.5mm and radius 8mm. The pressurization of the system is supported by means of a balloon located downstream the test section. A pressure control device is used to finely control this downstream pressure (P_{down}) in the installation. Various pressure and temperature sensors are used to determine precisely the test conditions. Here it is important to mention the definition of the cavitation number σ, used in the present paper:

$$\sigma = \frac{P_{down} - P_v}{P_{up} - P_{down}} \approx \frac{P_{down}}{P_{up} - P_{down}}$$

where P_{down} and P_{up} are the static pressures upstream and downstream the test section and P_v is the vapour pressure of the liquid at the temperature of the experiment.

To visualize the cavitating flow the metal sample was replaced with a sample made of Perspex with suitable thickness to withstand the working pressure (see Fig. 1).A 45° mirror was fixed in front of the Perspex allowing for cavitation images to be collected by a high speed camera (Phantom® MiroM320S). The optic used was a Tamron® AF 90mm f/2.8 SP Di macro-lenses. As one camera was available and optical access was restricted by the design of the flow rig, only bottom view images could be collected. Thus, any three dimensional effects developing within the 2.5mm gap could not be identified; the images and their post-processing can only reveal the projected view of the cavitation cloud on the imaging plane. Two lights (Lupo® Spot Daylight 1200) were placed behind the mirror and in front of the Perspex allowing for sufficient illumination.

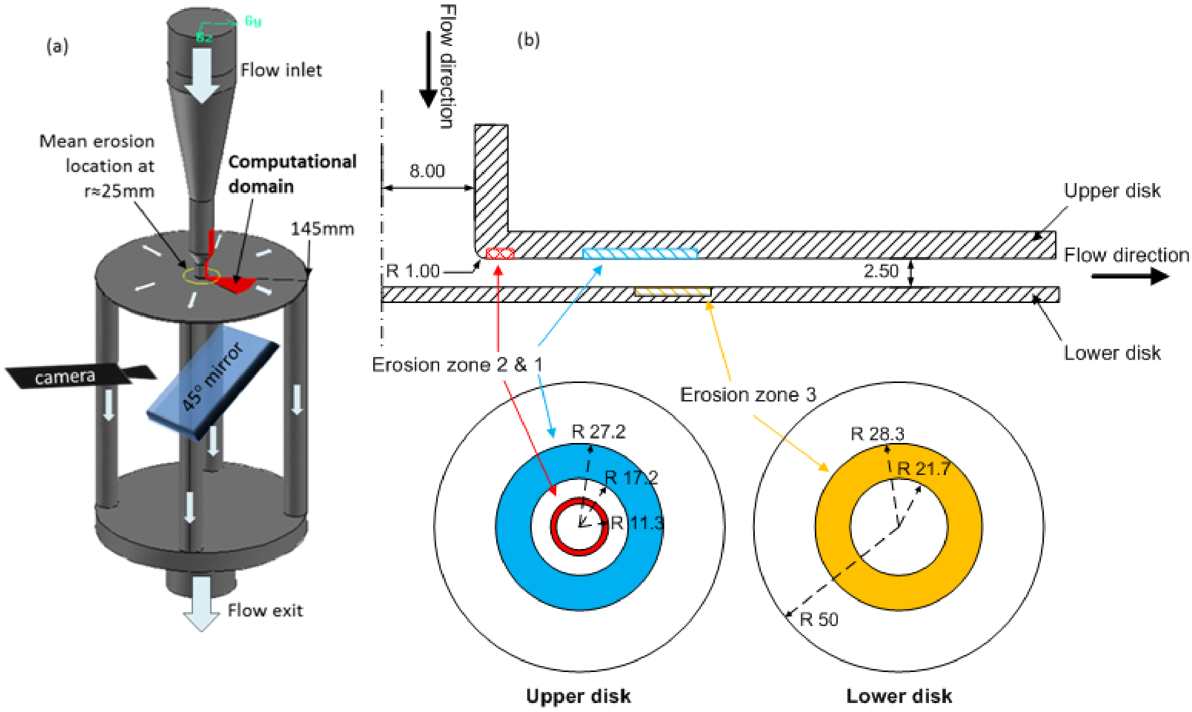

Fig. 1:(a) Sketch of the visualization apparatus from [15]. (b) Zoom-in to the area of interest; the dimensions of the three distinct erosion zones observed are indicated in mm, for σ=0.9.

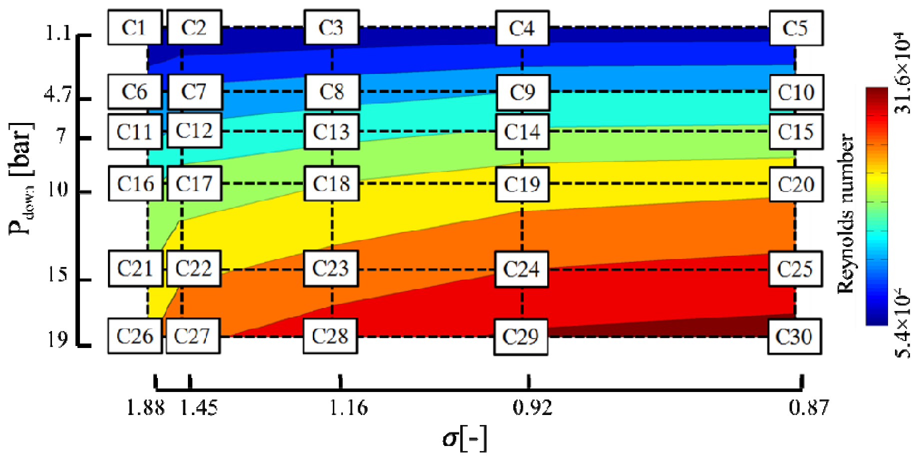

Table 1: The 30 test cases investigated. For each case, the experiment was conducted at fixed P_{down} and σ values. Note that both the p-axis and σ-axis are inverted. The Reynolds number is calculated between the two disks at r=25mm - see Fig. 1, based on the hydraulic diameter (D_h=5mm). The six cases at σ = 1.88 are not included in the experimental results, because a coherent cavitation cloud was not formed.

The area visualised was 34×16mm^2, so the pixel size was 132×125μm^2. This pixel size introduces an uncertainly of 0.4% (0.132/34) in the relative spatial resolution of the collected images. The videos were recorded at 77kHz with a resolution of 258×128 pixels. In total, more than 2000frames have been collected for each operating condition. The exposure time was set to 12μs; during that time the cavitation could move by less than 0.012mm, which is much smaller than the pixel resolution; practically this shutter time freezes the motion of the cloud. Visualisation tests were conducted at different cavitation numbers, σ from 0.8 to 1.90 and back pressures, P_{down} from 1.1bar to 19.1bar. The matrix of the test cases recorded is shown in Table 1. Flow conditions at the highest cavitation number (σ~1.9) correspond to cavitation inception at the given upstream and downstream pressure difference. Those cases are listed here for completeness although they have been excluded from the analysis to follow, as the cavitation cloud formed was very irregular and restricted to small cavitation pockets without any erosion data being reported. The Reynolds number indicated with the contour plot has been calculated on the basis of the hydraulic diameter of the 2.5mm passage and the mean flow velocity estimated at a radial distance of 25mm. From those conditions, the effect of σ and P_{down} can be evaluated separately. In this Table the numbering of the cases tested, from C1 to C30 is also indicated and this notation is used throughout the paper.

3. Flow structure and post processing methods

The cavitation cloud was found to change location rather transiently and non-axisymmetrically despite the steady-state operation and the axisymmetric geometry utilized; a typical sequence of the cloud formation and development is shown in Fig. 2. This figure shows representative images selected from case C29 of Table 1; this case corresponds to the erosion tests and sites described previously. The cloud is generated at the outlet of the feed nozzle; this has been a consistent observation for all cases recorded. Then the cavitation cloud grows as it is convected by the flow, until it reaches a maximum distance; this corresponds to the time frame of 0.117ms in Fig. 2. Upstream of this 'large-scale' cloud structure, which is indicated by the blue dotted line, a second 'large-scale' cloud, segmented by the red line is developing, flowing downstream in a similar manner. A cavitation-free zone is visible between them. The follow-up cloud is indicated by the green line and the process repeats itself in a clear vortex shedding mechanism. The estimated shedding frequency is of the order of 1 to 2 kHz for this particular test case; more details about the cloud collapse frequencies are assessed later on.

Having described the dominant flow structures, image post processing has been employed in an effort to provide estimates of parameters relevant to the spatial and temporal development of the cavitation clouds. To do that, the single-colour (grey-scale) images of cavitation recorded (a representative image is shown in Fig. 3a)are turned to binary ones; an example is shown in Fig. 3b. This has been achieved by utilizing the Otsu's method [29]; the threshold value chosen aims to minimize the interclass variance of the black and white pixels. Two averaging procedures have been performed: (a) per pixel and (b) along the circumferential direction, as indicated in Fig. 3b. The field of view analysed is an annular sector with radii 8 mm<r<30 mm and angle θ of 30 degrees. This zone has been divided into 260 concentric arcs.

At the outlet of the feed nozzle, light reflection on the radius of curvature may not be distinguished from the automatic process converting the raw images to binary ones. For this reason, this area has been masked up to a radial distance of 9.5mm and the corresponding pixels found in this angular zone have not been considered in the post-processing. For the point (pixel) averaging, the temporal mean cavitation presence and its standard deviation have been estimated and contour plots similar to Fig. 3c will be presented in the following section. The mean value can be interpreted as the % number of frames when cavitation is present in a particular location while the corresponding values of standard deviation indicate locations where unsteady cavitation develops.

Obviously, an error is introduced by the threshold value when performing this process. As possible acceptable threshold values can range between two extremes, the maximum relative error can be estimated and its spatial distribution is shown by the contour plot of Fig. 3c for case C27; this case has been selected as it exhibits less cavitation, and it has been found to have the maximum error among all cases investigated. It can be seen that the error can take value of up to 20% relative to the mean value of this particular case. The peak values exist in the central part of the cloud development as in these areas it is less accurate to draw clear boundaries between the cavitating and the non-cavitating areas. This error decreases with increasing radial distance and becomes smaller than 5% in the area of cloud collapse.

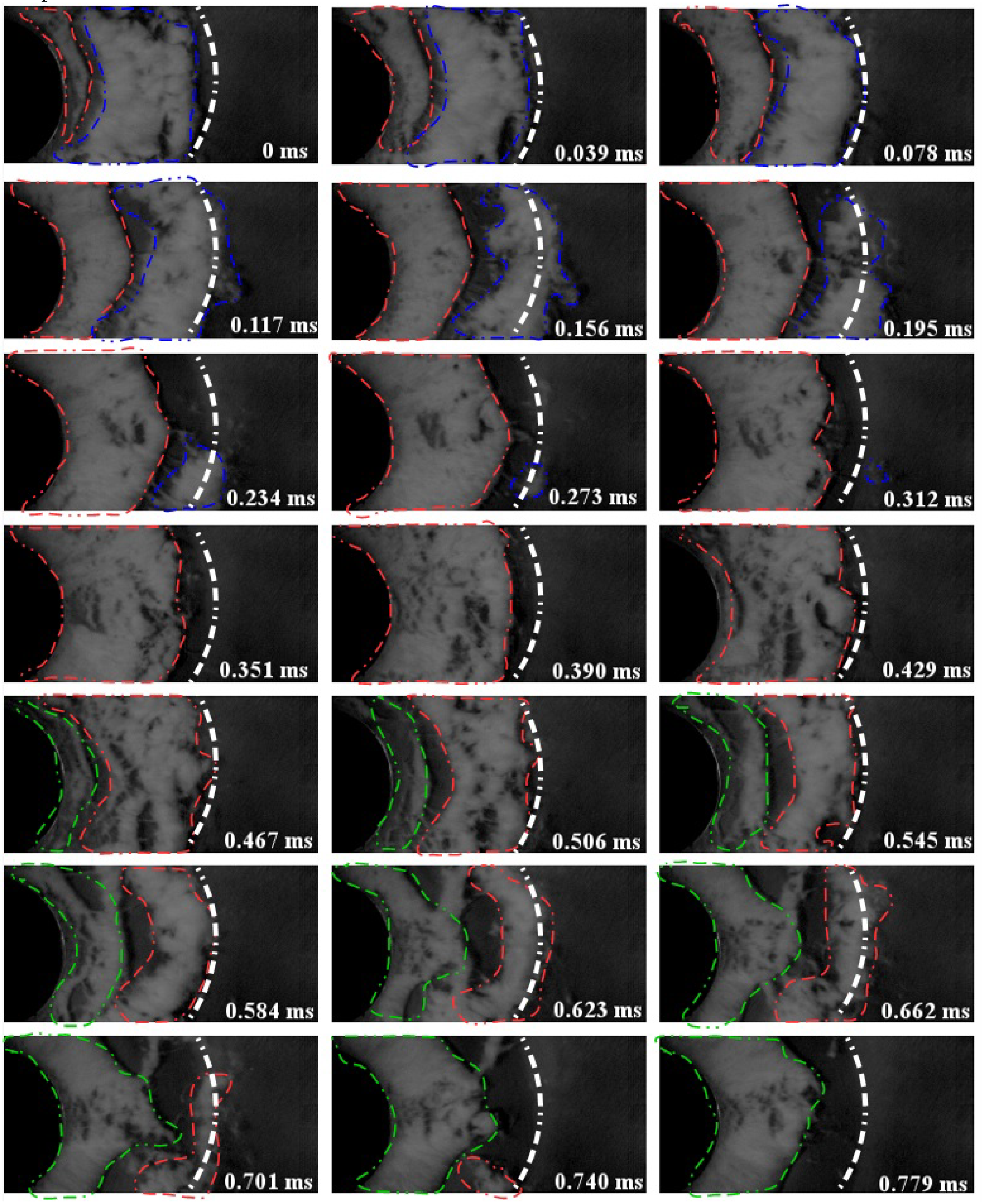

Fig. 2: Sequence of representative images captured using a frame rate of 77k frames per second (termed as fps from now on), C29 (P_{down} =19 bar, σ=0.92). The white dashed line indicates the

distance of 25mm from the axis of symmetry, which corresponds to the mean distance where erosion sites 2 and 3 have been observed. The coloured dashed lines follow the edge of successive cavitation clouds.

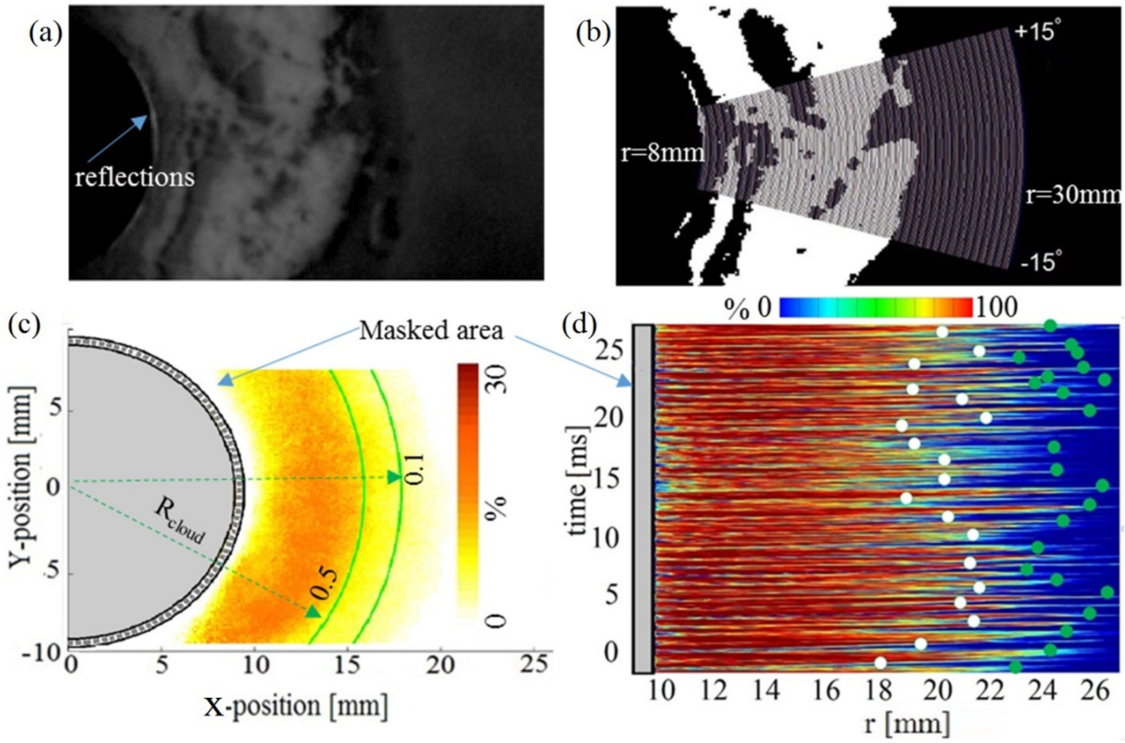

Fig. 3: (a) Representative raw image, (b) binary image after applying a threshold method; the circumferential sectors utilised for post-processing are superimposed. (c) Representative spatial distribution of relative error of the mean cavitation presence in every pixel visualised for case C29; the green lines indicate the cloud length by utilising two different threshold values of 0.5 and 0.1 for its estimation. (d) Representative plot of temporal evolution of the % circumferential area occupied by cavitation as function of distance from the axis of symmetry; the superimposed green circles indicate the locations of maximum cloud extend at the start of collapse and the white circles indicate the cloud length at the end of collapse.

The second image post-processing method employed estimation of averages along the circumferential direction. This time, the mean of the binary values along each arc has been obtained for every time instant recorded; this can be simply expressed as $N_1 / (N_0 + N_1)$, where N_0 is the number of pixels exhibiting zero value (no cavitation presence) and N_1 is the number of pixels with value equal to one along the selected areas. This ratio represents the percentage area of this circumferential sector occupied by cavitation at a given time step. A representative result from this process is shown in Fig. 3d.A few sample points (for clarity of the plot), indicated by the white and green circles, have been superimposed. These circles correspond to radial distances where the mean of the binary values across a circumferential sector has a value of 0.5, indicating that half of this sector is occupied by cavitation at a given time step. This parameter can be utilised to estimate the cloud length at the beginning and ending of the collapse phase. The white circles correspond to time instances at the end of the collapse phase while the green circles at the start of the collapse when the cloud has its maximum extent. By averaging the radial locations corresponding to these two time events, one can obtain the mean of the maximum and minimum cloud extend over all collapse cycles recorded. This is defined here as ‘cloud length’, and represented with R_{cloud}, and its variation for all cases is presented later on. The maximum value of R_{cloud} is also indicated on Fig. 3c by the green lines superimposed on this plot for this particular case C27. The one to the left has been estimated by using a value of 0.5. Obviously, other values towards zero could have been selected. However, with smaller values one may capture only small clouds isolated from the main cavitation area, and which may not be representative of the mean value across the whole circumferential area. As it is impossible to have an ‘accurate’ estimate, a relative error has been estimated by using a value of 0.1 (implying that only 10% of the circumferential sector is occupied by cavitation at a given time). The value calculated from this assumption is also indicated on Fig. 3c. It can be seen that the cloud length in this case is approximately 2.5mm further downstream relative to the value estimated when 0.5 was used. This gives a relative error of approximately 15% for this particular case. It decreases in cases with more cavitation to levels of around 1-1.5mm which corresponds to about 7% of the cloud length. Finally, fast Fourier transformation (FFT) applied to the temporal evolution of this cloud length can reveal the ‘large-scale’ cloud collapse frequency.

4. CFD Simulations

In the absence of quantitative velocity measurements in this configuration, CFD simulations have been performed to provide more insight to the flow structure. The described case was simulated using the in-house CFD solver, GFS. The solver is based on the finite volume methodology. The liquid phase is considered as an incompressible liquid and is resolved in an Eulerian reference frame, whereas cavitation is treated as a discrete phase tracked in Lagrangian frame of reference [30].The bubble motion is governed by the forces due to bubble/liquid interaction, whereas appropriate source terms are added in the continuous phase conservation equations to take into account the effect of the bubble presence inside the liquid flow. The bubble size is governed by the Rayleigh-Plesset equation [30]. The bubble number density for the cavitation inception was set to 10^{13}bubbles/m^3, with a size ranging from to 0.5μm to 2μm, following a logarithmic distribution; the aforementioned values are based on literature references [30, 31] and are considered representative of feed water. Since simulating explicitly all bubbles inside the volume would require enormous computational resources, parcels of bubbles are simulated; all bubbles within a parcel are assumed to behave in exactly the same way, thus they have the same velocity field and bubble radius and parcels are introduced in regions where the local pressure is below the saturation (the interested reader is addressed to [30]). In the present simulations the maximum number of bubble parcels was ~45000. The solver is capable of predicting the flow pattern of the fluid/vapour mixture, but, even if the bubbles may expand or collapse, cannot handle compressibility effects and pressure wave propagation in the bubbly medium.

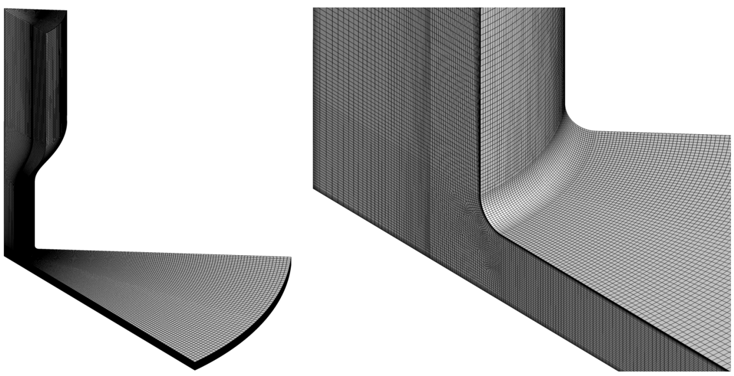

Fig. 4: Computational grid utilized for the CFD analysis; the grid consists of 1.4million cells and has a higher density at the cavitating region

The simulation performed with GFS was done with a hybrid RANS/LES model [32-34], since it was found that standard traditional URANS models fail to predict the vortex shedding mechanism, while also underestimate the size and the extents of the cavity; this is supported also from other CFD studies in the literature [27, 28]. Moreover, computational predictions with the RANS/LES model suggest the existence of a secondary nucleation site downstream the turn; such fine features are not captured by standard RANS models, as e.g. the k-epsilon model (see Fig. 5 -the comparison is made after obtaining a steady state solution using the k-epsilon model, whereas an average solution has been extracted from the transient hybrid RANS/LES approach, after sampling 550 time instances). While the prediction of a secondary nucleation site cannot be verified by experimental observations, due to the complexity of the flow field, the prediction of this site may contribute to the understanding of the underlying mechanisms of cavitation development and suggests further examination in future experiments. The predicted location of the second inception site is within the erosion free zone, lying between 11.3 and 17.2mm (see also Fig. 1), could be considered as a rough indication of agreement between the CFD and the experimental results. It must be highlighted here that it is not implied that the secondary cavitation inception region, downstream the turn, is a stationary vortex core; it appears in such a way, due to the time averaging process for many time instances. In practice, the secondary inception site is a highly dynamic and transient feature, generated by the high vorticity downstream the turn, spanning from a radius of 9 to 20 mm, see also **Σφάλμα! Άγνωστη παράμετρος αλλαγής.** and Fig. 10. This area has the form of a Rankine vortex, with a characteristic size of ~1.5mm.In order to simplify the simulation and decrease the computational cost, due to spatial and temporal resolution requirements of the turbulence model used, only 1/8th of the complete geometry was simulated (see Fig. 1). The computational mesh used consists of approximately 1.4million purely hexahedral cells, refined near the walls and the inlet sharp turn at the feed nozzle exit as showed in Fig. 4. The minimum cell size in the near wall vicinity is 2μm and the maximum dimensionless wall distance (y^+) in the area of interest is ~10. From the results obtained, it was tested that the turbulent kinetic energy spectrum obeys the Kolmogorov -5/3 law [35] and the highest temporal frequency was at least 10 times less than the sampling frequency; thus both the temporal and spatial discretizations were considered adequate for the simulations. The simulated condition was for P_{up}=40bar and P_{down}=19bar (pressure difference 21bar), corresponding to a flowrate of 8.16 l/s and a cavitation number of 0.92 (case C29 of Table 1). The discharge coefficient C_d, defined as:

$$C_d = \frac{Q_{CFD/Exp.}}{\sqrt{\dfrac{2(P_{in} - P_{out})}{\rho\left(\dfrac{1}{S_{out}^{\ 2}} - \dfrac{1}{S_{in}^{\ 2}}\right)}}}$$

is ~0.13 for the cavitating case. Simulating the same case and ignoring cavitation effects results to a significantly lower pressure difference prediction of ~13bar (C_d~0.16) instead of 21bar (reduction of 38%).

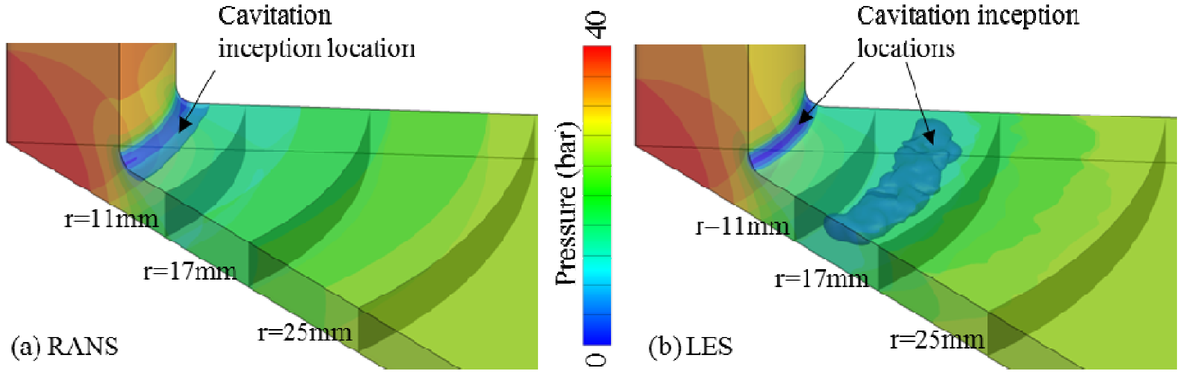

Fig. 5: Comparison of the pressure field from the RANS and the hybrid RANS/LES (averaged in time). The blue iso-surface denotes the region where pressure drops below saturation pressure. The simulation conditions correspond to C29, with σ~0.9 and P_{down}=19bar.

In Fig. 6 the velocity field at a slice of the computational domain is shown. The velocity field is highly unsteady, with vortices formed downstream the sharp turn, in the shear layer that develops at the boundary of the separated region. Pressure at the vortex cores drops below the saturation pressure, leading to the formation of vapour cavities, which travel downstream forming the cavitation clouds, in a similar pattern as shown from experimental results.

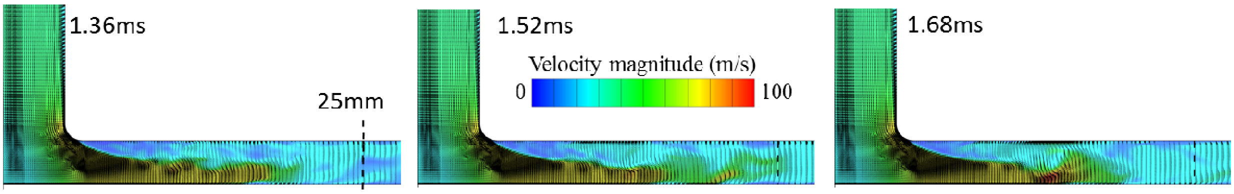

Fig. 6: Velocity distribution at three instances with a time interval of 60μs, taken at the middle slice of the simulated geometry. The simulation conditions correspond to C29, with σ~0.9 and P_{down}=19bar.

In Fig. 7 the instantaneous pressure distribution in the gap between the two disks is shown. Evidence of travelling vortices can be found here; as shown, pressure drops below saturation at the vicinity of the turn (primary inception point) and at the vortices formed due to the shear layer instability, downstream the turn. Collectively, these vortices act as the secondary nucleation site mentioned above. In both nucleation sites, bubble parcels are introduced, in order to take into account vapour presence in the flow field.

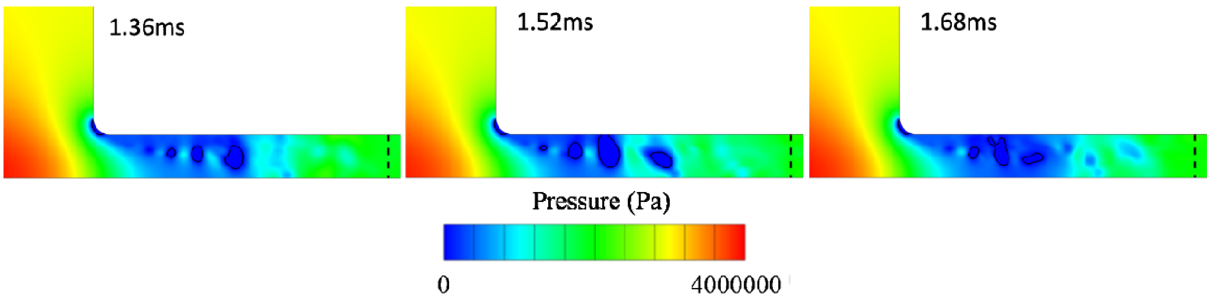

Fig. 7: Instantaneous pressure distribution at three instances with a time interval of 60μs, at the middle slice of the simulated geometry. The continuous line denotes the region where local pressure is below the saturation pressure and the dashed line the radius of 25mm.

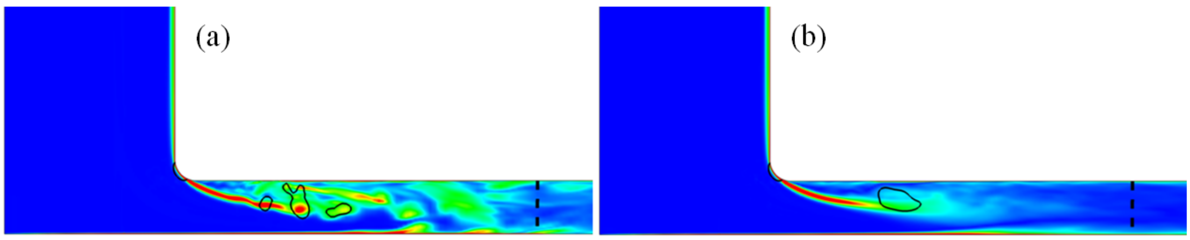

Fig. 8: (a) Instantaneous and (b) time-averaged vorticity magnitude fields. The continuous line shows the inception sites, with local pressure lower than the saturation pressure, whereas the dashed line indicates the radius of 25mm. Note that, due to interpolation during the slice extraction, smoothing is inevitably introduced to the vorticity field.

Furthermore, the CFD results provide an indication of the driving mechanism of the cavity shedding. Indeed, as shown in Fig. 9, the mechanism of the cavity detachment seems to be the re-entrant jet formed between the cavity and the adjacent wall. To be more specific, the cavities formed at the primary inception point at the turn are unstable, thus at some point, a re-entrant jet is formed, starting from the cavity closure location, which forces the cavity to separate from the wall. During the cavity separation, significant vorticity is generated due to the opposing directions of the bulk of the flow and the re-entrant jet. Afterwards, the cavity travels downstream while it may grow further, due to the influence of vorticity. Analysis of the flow field using sampling probe points and performing FFT shows frequencies beginning from 2500Hz till 25000Hz.

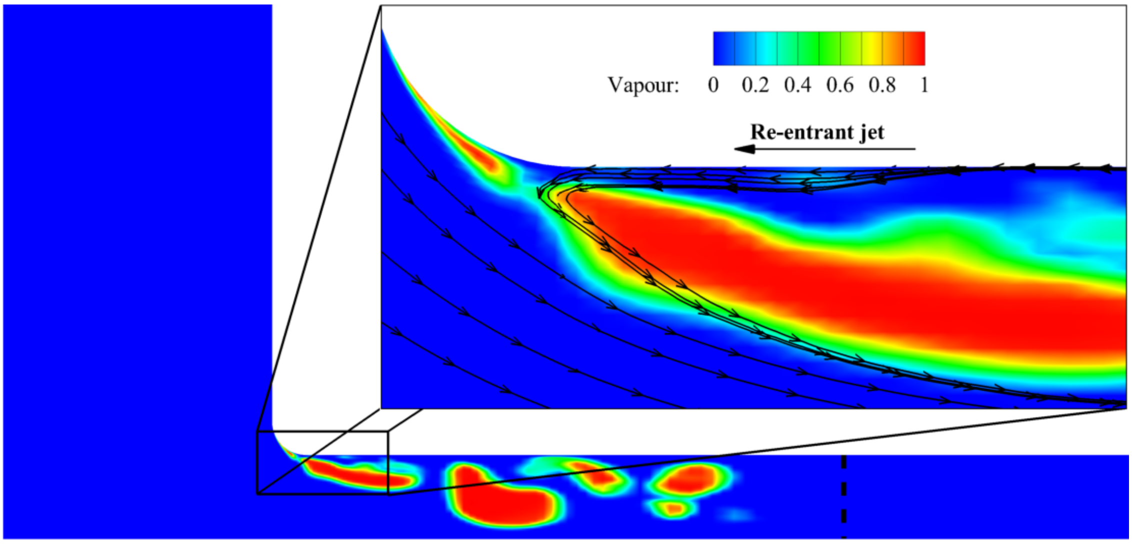

Fig. 9. Detailed view during the detachment of a vapour cavity. The effect of the re-entrant jet is visible in the zoomed in region. The contour denotes the vapour fraction and the dashed line denotes the radius of 25mm.

In

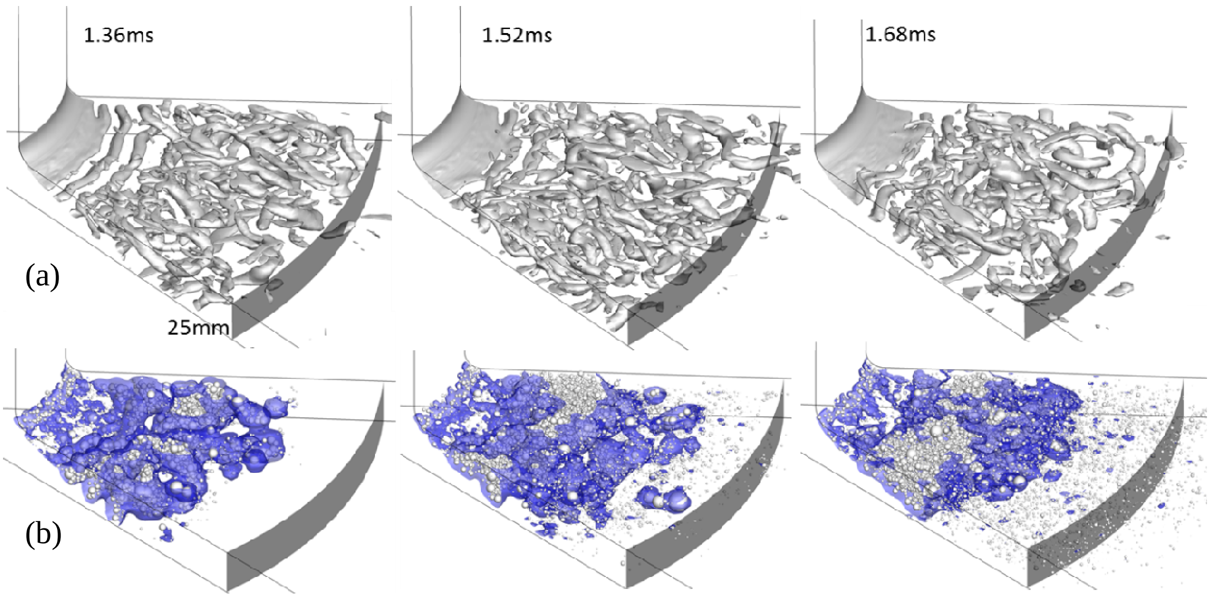

Fig. 10a, the vortical structures formed due to the flow direction change are shown. For the representation, the second invariant of the velocity vector was used [36]. From the results, it is found that vortex tubes are formed after the sharp turn, organizing in filament-like structures (similar structures are found from the experimental results as well, e.g. at Fig. 2 at 0.506-0.545ms at the vicinity of the nozzle exit), which are convected by the flow and, later on, merge into more complicated structures. Pressure at the vortex cores may drop below the saturation pressure, thus forming moving cavitation inceptions sites. Eventually, vortices are dissipated due to the fluid viscosity, resulting to the collapse of vapour structures. The corresponding plots for the cavitation bubbles utilised and the resulting vapour volume fraction iso-surface of 0.5 is indicated in Fig. 10b.

Comparison of those results against the images of the previous Fig. 2, is shown in

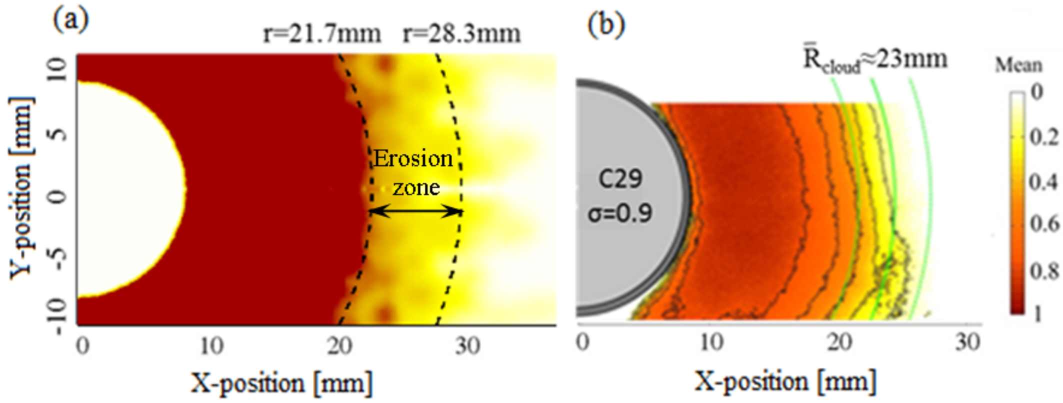

Fig. 11(σ=0.9and P_{down}=19bar) where the time averaged probability of vapour presence is shown for both the experiment and the hybrid RANS/LES results, projected on the lower disk; the probability was estimated based on a threshold value which was 5% vapour fraction for the CFD calculations (i.e. if the average vapour fraction at the line of sight is more than 5%, then the probability is 1, else it is zero).The comparison indicates similar locations of bubble cloud formation and collapse regions, e.g. the vapour structures begin to collapse at ~20mm from the axis of symmetry (see Fig. 10) and may disappear just after the 25mm.Regarding the vapour distribution in the normal direction between the two disks no experimental data are available. However, on average, the vapour distribution from the CFD results shows a stronger vapour presence near the upper disk and this could possibly correlate to the extended erosion zone found at the specific disk.

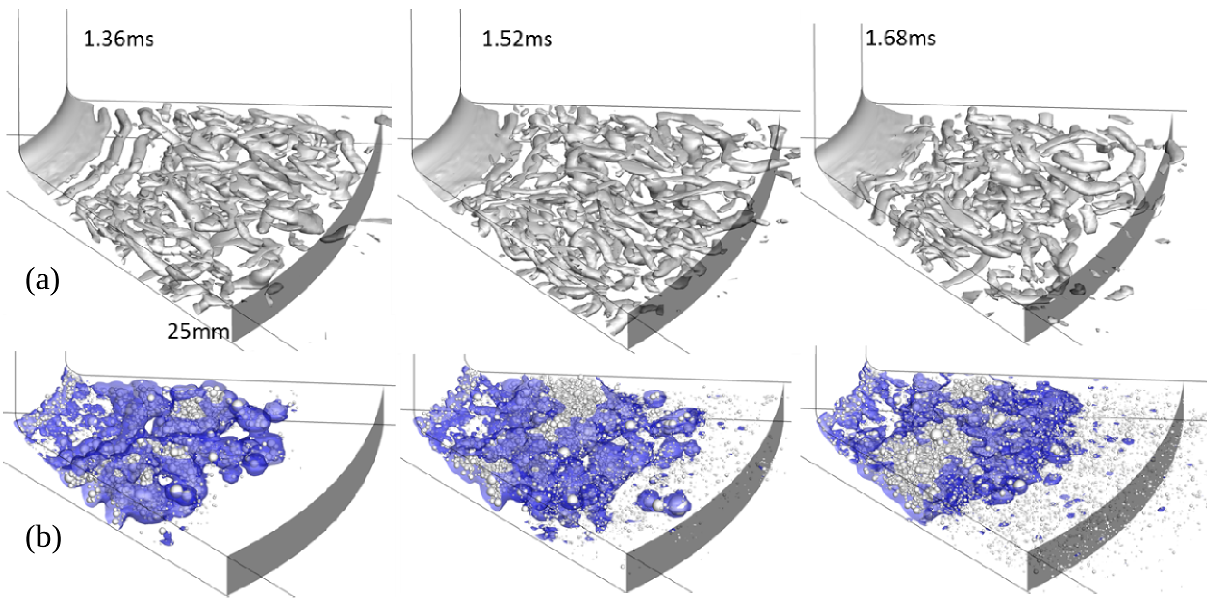

Fig. 10: (a)Vortical structures, indicated with the second invariant of the velocity gradient tensor and (b) representative bubble parcels utilized for the simulation of cavitation; the blue iso-surface corresponds to cavitation volume fraction of 0.5. The simulation conditions correspond to C29, with σ≈0.9 and P_{down}=19bar.

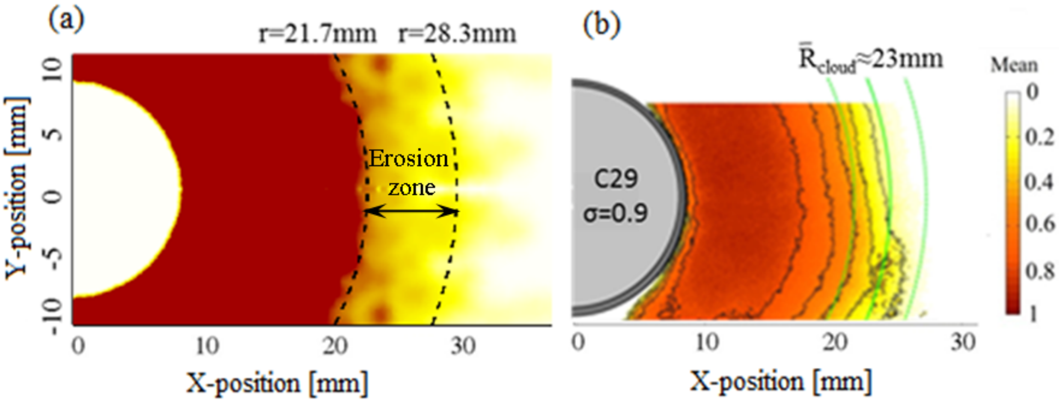

Fig. 11. (a)Time averaged vapour probability distribution from the CFD calculations, for case to C29, with σ~0.9 and P_{down}=19bar. The dashed lines represent the area of erosion of the lower disk for the specified cavitation number. The region of erosion coincides well with the collapse of the vapour structures. (b) The average experimental vapour probability distribution.

5.Spatial mean cavitation distribution and cloud length

Having described the flow development we now proceed to the presentation of the results obtained from the post-processing of the collected images. The first series of results is presented in Fig. 12. It shows the spatial distribution of the temporal mean cavitation presence and its standard deviation for selected operating conditions of Table 1. In each plot, the feed inlet area corresponds to the circle in the middle of the picture. As mentioned earlier, concentrically with it, a thin zone has been plotted without any value. This was because in the area of inlet, light reflections have prevented the collection of clear images and, thus, the cavitation could not be distinguished automatically.

A general remark from Fig. 12is that there is a slight asymmetry in the time averaged results. This is believed to be caused by the asymmetry induced by the outlet pipes. As shown in Fig. 1a, the geometry of the device is not entirely axisymmetric at the outlet of the disks gap; there are four outlet pipes that are positioned every 90degress. These pipes probably induce a disturbance in the velocity field, imposing a direction of preference, which is manifesting at the lower part of the spatial distributions in Fig. 12, for a X-position of ~25mm. For the time being, it is not possible to quantify the exact effect of the outlet pipes or upstream effects (pipe bends) in the induced asymmetry of the flow field.

The effect of cavitation number, σ, can be realised from Fig. 12b. This parameter has an appreciable effect on the extent of cavitation. For high cavitation numbers, mean values have a maximum of less than 50%, which implies that most of the running time no cavitation is present. With decreasing σ, both the appearance becomes more frequent and the cloud propagates further into the flow. For sufficient enough pressure difference, the cloud reaches a ‘steady-state’ condition and it does not extend further in the radial direction. The erosion sites 2 and 3, as shown in the previous Fig. 1b coincide well with the estimated cloud length, which effectively indicates the area where the cavitation cloud collapses. This zone coincides well with the area of high standard deviation values. Effectively, this area is exposed to successive cloud collapse events. Fig. 12a presents the same parameters but this time the cavitation number has been kept constant and the back pressure is changing. It is clear that changing the back pressure has only marginal effect of the cavitation development when σ is kept constant. The cloud length is indicated with the solid green line while the corresponding standard deviation is indicated with the green dotted lines residing to the left and right of the solid one. The estimated cloud length values are also shown on Fig. 13as function of the cavitation number for all back pressure conditions investigated; the standard deviation is also indicated with the vertical bars for all operating points. A clear trend is observed: the cloud length decreases linearly with σ, while there are no significant variations with back pressure.

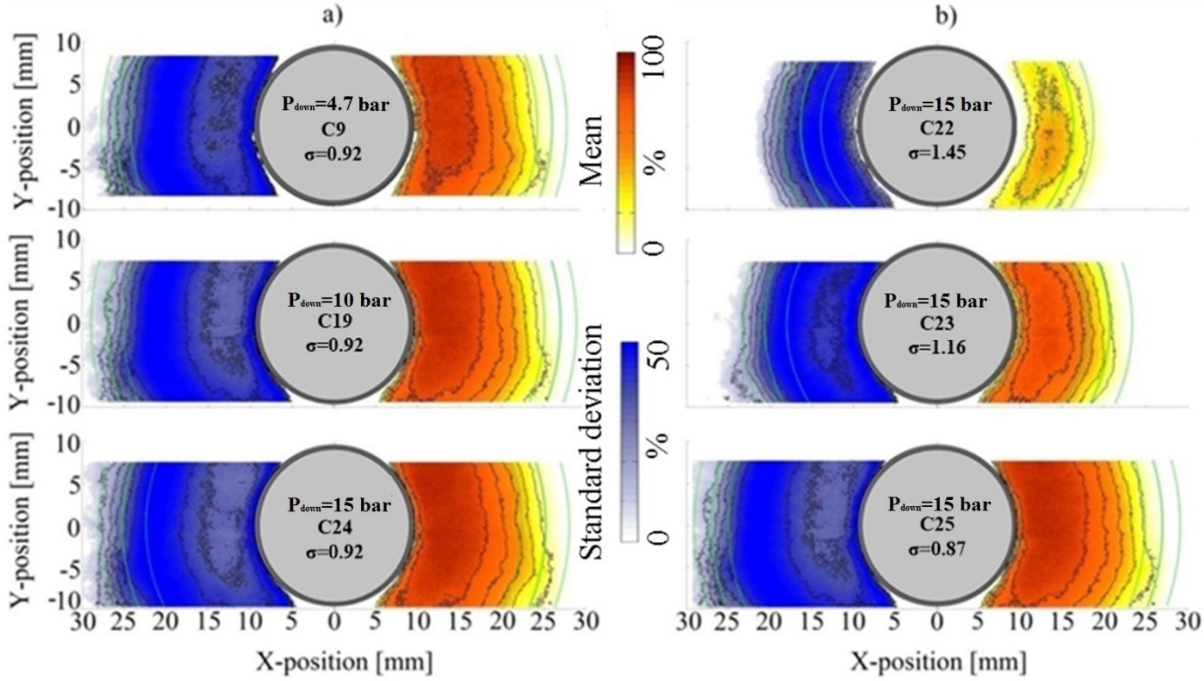

Fig. 12: Spatial distribution of the mean (time averaged) and its standard deviation (expressed as % of the mean) of cavitation presence in the visualised area. The green solid line indicates the temporally mean cloud length and the green dotted lines indicate its standard deviation. (a) Effect of back pressure for fixed cavitation number (cases C9, C19, C24). (b) Effect of cavitation number for fixed back pressure (cases C22, C23, C25of Table 1).

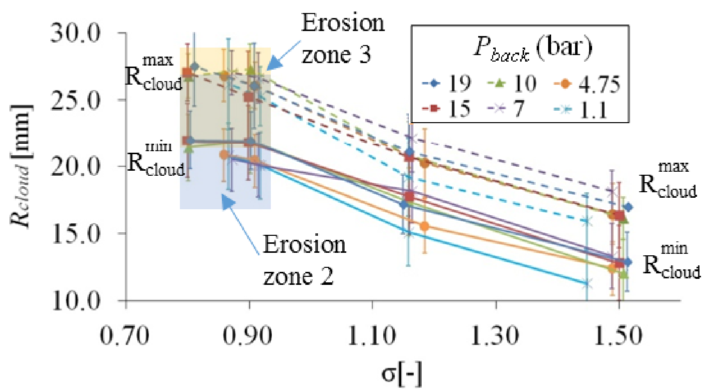

Fig. 13: Maximum (dashed lines) and minimum (solid lines) cavitation cloud length as function of cavitation number σ for different downstream pressures; the extent of the erosion zones 2 and 3 for a cavitation number of ~0.9 (see Fig 1) are also superimposed.

6. Temporal development of cavitation cloud and shedding frequency at location of collapse

Having described the development of cavitation and its mean distribution, we proceed now to presentation of results revealing more information about its temporal development. In particular, results obtained by utilising the averaging procedures along the circumferential direction, as described earlier, are presented in Fig. 14. The corresponding temporal variation of this mean value is plotted as function of the radial distance from the inlet. The conditions of Fig. 14a correspond to the same cavitation number σ=0.92(cases C9, C19 and C24 of Table 1) while plots of Fig. 14b correspond to conditions where the cavitation number is changing and the back pressure has been kept constant (cases C22, C23 and C25 of Table 1).

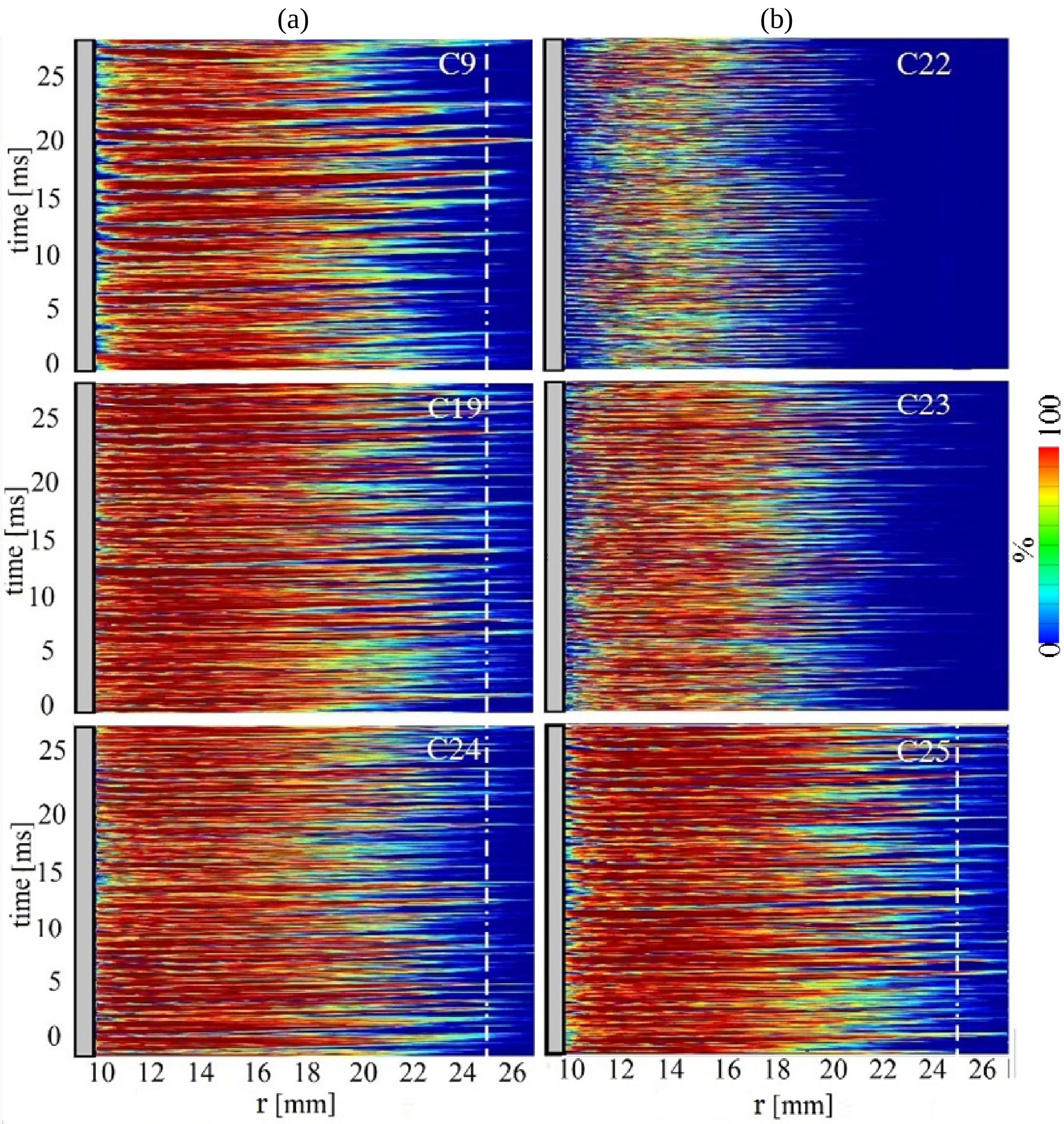

Fig. 14: Temporal variation of the circumferentially mean cavitation presence as function of the distance from the axis of symmetry. (a) Effect of back pressure for constant σ (cases C9, C19 and C24 of Table 1) and (b) effect of σ for constant back pressure (cases C22, C23 and C25 of Table 1). The vertical dotted while line indicates the mean erosion position of 25mm, visible only in cases where the cavitation number is ~0.9.

From these plots, it is possible to evaluate the frequency of the cloud appearance/disappearance and collapse. In particular, it is of interest to estimate the main cloud frequency, f_{cloud}, at the distance of 25mm which corresponds to the erosion sites 2 and 3 and the corresponding Strouhal number. The f_{cloud} has been evaluated by the fast Fourier transformation (FFT)and it is shown in Fig. 15a for all operating conditions tested. It becomes apparent that CFD predictions of the flow field frequency is higher than that of the experimental shedding frequency. However, direct comparison of the temporal frequencies between the experiment and CFD is not straightforward, since the flow field was not obtained from the experiment; experimental frequencies were calculated based on the macroscopic flow features, without taking into account the intricate temporal fluctuations of the flow field. Similar to past observations of cavitation cloud shedding (for example, [18]) the clouds at high σ are small and detach/collapse frequently, whereas at low σ the clouds grow and collapse at a slower rate. The f_{cloud} increases with increasing downstream pressure, due to increase of the flow velocity. This frequency of collapse at the distance of R_{cloud} as plotted here is similar to the frequency of formation of the 'large scale' clouds as estimated earlier from the raw images of Fig. 2. Finally, Fig. 15b shows the Strouhal number, estimates using as length scale the cloud length and the mean velocity of the flow at this location. It is noticeable that the Strouhal number seems to be relatively constant for all tested conditions.

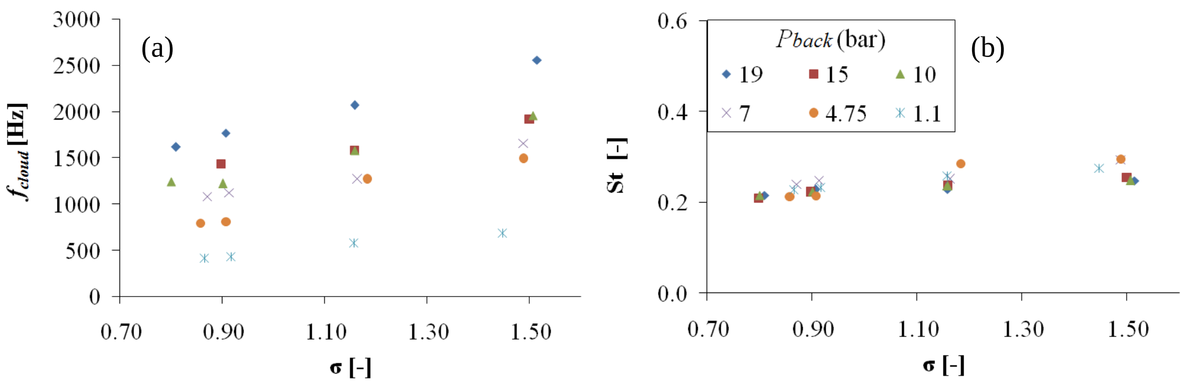

Fig. 15:(a) Cloud collapse frequency (f_{cloud}) at 25mm from the axis of symmetry, as function of σ for different downstream pressures (P_{down}). The main frequency has been evaluated utilizing the power spectral density criterion [37]. (b) Strouhal number estimated using the f_{cloud}, the disk distance (2.5mm) and the corresponding mean flow velocity at a radius of 25mm.

7. DISCUSSION OF RESULTS

Both experimental and computational results show an intricate flow field occurring inside the device; indeed, the flow is highly unsteady showing a periodic behaviour which varies depending on the cavitation number,σ, and Reynolds number, *Re*. At high cavitation numbers cavitation is not well defined, that is no coherent cavitation structures are formed. As cavitation number decreases, the cavitation influence becomes more significant; cavitation becomes more intense and extends at a larger area, from the nozzle exit to a maximum radial distance of almost 30mm (see Fig. 14). The effect of Reynolds number is primarily linked to the shedding frequency of the cavitation structures; indeed, when considering a constant cavitation number σ, at low back pressures (which also corresponds to low Reynolds number) the shedding frequency is lower. On the other hand, as the downstream pressure is increased, for constant cavitation number σ, the frequency of the shedding also increases.

When considering a constant downstream pressure, decrease of the cavitation number results to a lengthened and more regular cavity which detaches at lower frequency, while increase of the cavitation number results to smaller and more unstable cavities forming and collapsing at higher frequencies. While this looks counterintuitive, since the decrease of the cavitation number results to increased Reynolds number and, theoretically, to a higher frequency, it is justified by the fact that at low cavitation numbers cavitation structures live longer thus have the time to form agglomerations. In that case, individual vortex cavities are impossible to distinguish, giving the impression of a lower shedding frequency. Contrary, at higher cavitation numbers at similar Reynolds (thus at higher downstream pressures), cavities tend to remain separate, thus the apparent frequency seems higher.

The dependence of the Reynolds number on the frequency is justified by the increased vorticity that is being generated downstream the turn. As it was shown from numerical results, the shear layer that forms downstream is unstable and generates significant vorticity. The increase of the Reynolds number with the corresponding increase of the velocity increases the rate of generation of vortices and consequently the frequency of shedding of the resulting cavitating structures.

A complementary explanation of the unsteadiness of the cavitation shedding process, supported by CFD results, is the influence of the re-entrant jet, formed at the vicinity of the cavity closure; the re-entrant jet has been identified also in the literature as a feature driving the flow unsteadiness for both internal and external flows, e.g. [38, 39]. The distinct phases of the cavity growth and detachment are described below(also shown schematically in Fig. 16);

1) Initially cavitation forms at the turn (primary inception site, see also the description in CFD simulations section), due to the rapid acceleration of the liquid.

2) The cavity stretches over time due to the local flow conditions, i.e. the shear and the drag, displacing liquid.

3) The closure of the cavity is a saddle point [40], thus its location is highly unsteady. A re-entrant jet is formed, which pushes the closure point back towards the turn. The cavity begins to separate from the adjacent wall.

4) The re-entrant jet detaches the cavity from the wall, while impinging on the primary inception site.

5) The cavity is entirely detached from the primary inception site and the rear part transforms into a bubble cloud. Around the cloud there is significant vorticity, due to the momentum of the re-entrant jet, which is in the opposite direction of the main flow. Moreover, the primary inception site starts to collapse, thus causing erosion at the vicinity of the turn (erosion zone 2).

6) The detached cavity transforms into a bubble cloud and moves downstream following the flow. It rapidly rotates due to aforementioned circulation, thus its pressure may fall below saturation and continue to grow, acting as the secondary inception site. The cycle is repeated from (1).

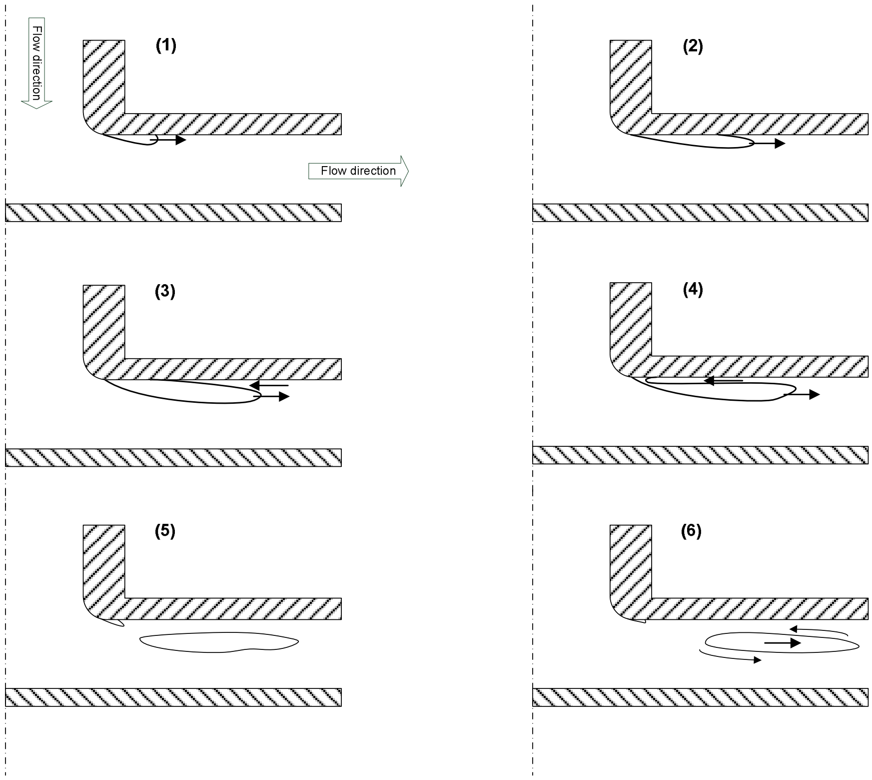

Fig. 16. The cavity shedding cycle: (1) a cavity is formed at the nearby region of the turn, (2) the cavity extends due to shear with the surrounding fluid, (3) the elongation of the cavity stops, while a re-entrant jet is formed, (4) the re-entrant jet detaches the cavity from the adjacent wall, (5) the vapour cavity is entirely detached from the parent cavity at the turn, (6) the detached vapour cavity follows the flow and travels downstream, while it may expand even more due to vorticity.

The growth and collapse of the vapour clouds is speculated to be linked to the compressibility effects that occur in cavitating flows. Indeed, it is known that the bubbly mixture of vapour/liquid is highly compressible. As mentioned above, a series of vapour cavities is shed from the primary inception site at the turn. These vapour cavities form collectively the bubble cloud, as shown in Fig. 2. As the bubble cloud is travelling downstream, pressure is recovering and vorticity is dissipating due to viscosity. Once the surrounding pressure force counteracts the vorticity induced centrifugal force, the edge of the bubble cloud, approximately at a radial distance of 25mm from the axis of symmetry, starts to collapse. The collapsing bubble cloud may cause a cascade of pressure waves, due to the rapid deceleration of the surrounding water, which could contribute to the erosion in zones 1 and 3.

8. CONCLUSIONS

Visualization and CFD results of the cavitation cloud developing inside a hydraulic device have been presented, providing more insight into the details of the sheet/cloud cavitation development for the flow conditions where previous data on material's response to cavitation erosion have been recorded[1]. As shown from the visualization experiment, the dynamics of the cavitation clouds are complex. In all cases examined, the cloud is generated in the vicinity of the outlet of the feed nozzle. Then the cavitation cloud grows up and is convected by the flow, until it reaches a maximum distance, which varies over time. Afterwards, the cloud collapse is followed by successive formation of clouds. The erosion zones coincide with the areas corresponding to the maximum and minimum cloud length.

Despite the axisymmetric geometry utilized, instantaneous pictures of cavitation indicate variations in the circumferential direction. A slight deviation from axis-symmetry is found in averaged results too, which is attributed to the outlet piping of the device, which is not axis-symmetric. Image post-processing has been used to characterize in more detail the phenomenon. In particular, the mean cavitation appearance and the cavity length have been estimated, showing good correlation with the erosion zone. This also coincides with the locations of the maximum values of the standard deviation of cavitation presence. Cloud collapse length was estimated with an uncertainty of less than 10% and it was found to decrease fairly linearly with cavitation number. In addition, the dominant frequency of the 'large-scale' cavitation clouds has been estimated through FFT. Cloud collapse frequencies vary almost linearly between 200 to 2000Hz as function of the cavitation number and the downstream pressure but the corresponding Strouhal number remains almost constant for all conditions. It is speculated that pressure wave propagation affects the cavity shedding mechanism, creating the gaps in-between subsequent cavitation clouds.

The main correlations between the cavity length and shedding frequency with the downstream pressure and cavitation number are:

- The increase of the cavitation number gives smaller cavitation zones. At very high cavitation number, cavitation occurrence is sparse and in-coherent. On the other hand, decrease of the cavitation number leads to more coherent cavitation structures, extending at larger areas, from 9mm till almost 30mm. The cavitation number is the sole factor affecting the maximum extent of the cavity.
- The increase of the downstream pressure, for the same cavitation number, leads to an increase in the shedding frequency. This is due to the increase of the Reynolds number, which enhances turbulence and vortex shedding.
- The decrease of the cavitation number for a constant downstream pressure gives a reduction of the shedding frequency. This is explained by the fact that, at low cavitation numbers, individual cavitation vortices live longer and form agglomerates that are difficult to distinguish, thus giving the impression of a lower apparent shedding frequency.

From the CFD results, it becomes apparent that a mechanism similar to vortex shedding occurs. Indeed, significant vorticity is generated downstream the turn, organizing in vortex tubes and manifesting as filament-like structures. This was confirmed by the experimental observations, since similar thread like structures have been captured during the image acquisition process. There is indication that pressure inside the vortex cores may drop well below the saturation pressure, resulting to cavitation inception downstream the turn. The LES/RANS methodology used in the present work shows that there could be a secondary nucleation site downstream the turn; this site cannot be predicted by pure RANS methodologies but, at the present, cannot be confirmed by experimental observations, thus requiring further examination. However, it is noticeable that the erosion free zone, located in-between two erosion zones, coincides with the areas where CFD predictions indicated as the secondary cavitation inception site. The contribution of the pressure wave propagation within the bubbly medium is possibly a driving factor on the development of discrete cavitation clouds, but in the present cannot be taken into account, due to limitations of the modelling capabilities of the software used.

ACKNOWLEDGMENT

The authors would like to acknowledge the contribution of The Lloyd's Register Foundation. Lloyd's Register Foundation helps to protect life and property by supporting engineering-related education, public engagement and the application of research. Also, the authors would like to thank Michel Riondet for his valuable support during the experiments at Grenoble.

REFERENCES

[1] Franc JP. Pitting tests and Cavitation Intensity. Int workshop on Adv Exp & Num Tech for Cav erosion prediction. Grenoble2011.
[2] V. Kini, C. Bachmann , A. Fontaine, S. Deutsch, Tarbell JM. Flow Visualization in Mechanical Heart Valves: Occluder Rebound and Cavitation Potential. Annals of Biomedical Engineering. 2000;28:431-41.
[3] T. Van Terwisga LZ, P. Fitzsimmons, E. J. Foeth. Cavitation Erosion – A review of physical mechanisms and erosion risk models. Ann Arbor, Michigan, USA: Proceedings of the 7th International Symposium on Cavitation; 2009.
[4] J-K. Choi, A. Jayaprakash, Chahine G. Scaling of cavitation erosion progression with cavitation intensity and cavitation source. Wear. 2012;Article in Press.
[5] Wang JJ-A. An innovative low/high temperature, repetitive pressure-pulse apparatus fir cavitation damage research. Int workshop on Adv Exp & Num Tech for Cav erosion prediction. Grenoble2011.
[6] D.H. Mesa, C.M. Garzon, Tschiptschin AP. Influence of cold-work on the cavitation erosion resistance and on the damage mechanisms in high-nitrogen austenitic stainless steels. Wear. 2011;271:1372-7.
[7] LeLay F. Evaluation of the cavitation erosion resistance of polymeric coatings and materials. Int workshop on Adv Exp & Num Tech for Cav erosion prediction. Grenoble2011.
[8] Chahine G. Development of cavitation erosion prediction method and procedures. Int workshop on Adv Exp & Num Tech for Cav erosion prediction. Grenoble2011.
[9] A. Boorsma, Whitworth S. Understanding details of cavitation. 2nd ISMP conf. Hamburg, Germany2011.
[10] G. Bark, Bensow R. Decomposition of the hydrodynamics of cavitation erosion. Int workshop on Adv Exp & Num Tech for Cav erosion prediction. Grenoble2011.
[11] S. Hattori, Ishikura R. Revision of cavitation database and analysis of stainless steel data. Wear. 2010;268:109-16.
[12] S. S. Rajahram, T.J. Harvey, Wood RJK. Evaluation of a semi-empirical model in predicting erosion-corrosion. Wear. 2009;267:1883-93.
[13] A. Osterman, B. Bachert, B. Sirok, Dular M. Time dependant measurements of cavitation damage. Wear. 2009;266:945-51.
[14] M. Dular, Osterman A. Pit clustering in cavitation erosion. Wear. 2008;265:811-20.
[15] J. P. Franc, M. Riondet, A. Karimi, Chahine GL. Material and velocity effects on cavitation erosion pitting. Wear. 2012;274– 275:248– 59.
[16] Arndt R. Some remarks on hydrofoil cavitation. Journal of Hydrodynamics, Ser B. 2012;24:305-14.
[17] B. Huang, Y. L. Young, G. Wang, Shyy W. Combined Experimental and Computational Investigation of Unsteady Structure of Sheet/Cloud Cavitation. Journal of Fluids Engineering. 2013;135.
[18] M. Kjeldsen, R. Arndt, Effertz M. Spectral Characteristics of Sheet/Cloud Cavitation. J Fluids Eng. 2000;122:481-7
[19] Petkovšek M, Dular M. Simultaneous observation of cavitation structures and cavitation erosion. Wear. 2013;300:55-64.
[20] Rossinelli D, Hejazialhosseini B, Hadjidoukas P, Bekas C, Curioni A, Bertsch A, et al. 11 PFLOP/s simulations of cloud cavitation collapse. Proceedings of SC13: International Conference for High Performance Computing, Networking, Storage and Analysis. Denver, Colorado: ACM; 2013. p. 1-13.
[21] M.S. Mihatsch, S.J. Schmidt, M. Thalhamer, Adams NA. Quantitative Prediction of Erosion Aggressiveness through Numerical Simulation of 3-D Unsteady Cavitating Flows. In: Ohl CD, editor. CAV2012. Singapore 2012.

[22] J.J-A. Wang, Brennen CE. Numerical computation of shock waves in a spherical cloud of cavitation bubbles. Journal of Fluids Engineering. 1999;121:872-80.
[23] S. Van Loo, T. Van Terwisga, H.W.M. Hoeijmakers, Hoekstra M. Numerical study on collapse of a cavitating cloud of bubbles. CAV2012. Singapore2012.
[24] Z. R. Li, Terwisga TV. On the capability of multiphase RANS codes to predict cavitation erosion. 2nd ISMP conf. Hamburg, Germany2011.
[25] Li ZR. Assessment of cavitation erosion with a multiphase Reynolds-Averaged Navier-Stokes method: PhD Thesis, TU Delft; 2012.
[26] P. Genereux, S. J. Head, D. A. Wood, S. K. Kodali, M. R. Williams, J-M. Paradis, et al. Transcatheter aortic valve implantation: 10-year anniversary. Part II: clinical implications. European Heart Journal. 2012;33:2399–402.
[27] O. Coutier-Delgosha, J. L. Reboud, Delannoy Y. Numerical simulation of the unsteady behaviour of cavitating flows. International Journal for Numerical Methods in Fluids. 2003;42:527-48.
[28] O. Coutier-Delgosha, J. L. Reboud, Fortes-Patella R. Evaluation of the Turbulence Model Influence on the Numerical Simulations of Unsteady Cavitation. Journal of Fluids Engineering. 2003;125:38-45.
[29] Otsu N. A Threshold Selection Method from Gray-Level Histograms Systems, Man and Cybernetics, IEEE Transactions on 1979;9.
[30] Giannadakis E. Modelling of Cavitation in Automotive Fuel Injector Nozzles: University of London; 2005.
[31] Brennen CE. Cavitation and Bubble Dynamics: Oxford University Press; 1995.
[32] S. T. Johansen, J. Wu, Shyy W. Filter-based unsteady RANS computations. International Journal of Heat and Fluid Flow. 2004;25:10-21.
[33] J .Wu, Y. Utturkar, Shyy W. Assesment of modeling strategies for cavitating flow around a hydrofoil. Fifth International Symposium on Cavitation (CAV2003). Osaka, Japan2003.
[34] C. C. Tseng, Shyy W. Turbulence modeling for isothermal and cryogenic cavitation Aerospace Sciences Meeting Including The New Horizons Forum and Aerospace Exposition (47th AIAA). Orlando, Florida2009.
[35] Pope SB. Turbulent Flows: Cambridge Press; 2003.
[36] X. Jiang, Lai CH. Numerical techniques for direct and large eddy simulations: Chapman & Hall / CRC; 2009.
[37] S. Miller, Childers D. Probability and random processes. Academic Press. 2011.
[38] Goncalves E, Patella RF. Numerical simulation of cavitating flows with homogeneous models. Computers & Fluids. 2009;38:1682–96.
[39] Lange DFD, Bruin GJD. Sheet Cavitation and Cloud Cavitation, Re-Entrant Jet and Three-Dimensionality. Applied Scientific Research. 1998;58:91-114.
[40] Hunt JCR, Abell CJ, Peterka JA, Woo H. Kinematical studies of the flows around free or surface-mounted obstacles; applying topology to flow visualization. Journal of Fluid Mechanics. 1978;86:179-200.